Absolute stimulated Brillouin side scattering in an inhomogeneous flowing plasma

C. Z. Xiao,[1,2,3,*] Y. G. Chen,[1] J. F. Myatt,[2] Q. Wang,[2] Y. Chen,[1] Z. J. Liu,[4,5] C. Y. Zheng,[4,5,3] and X. T. He[4,5,3]

[1]*School of Physics and Electronics, Hunan University, Changsha 410082, China*

[2]*Department of Electrical and Computer Engineering, 9211 116 St. NW, University of Alberta, Alberta T6G 1H9, Canada*

[3]*Collaborative Innovation Center of IFSA (CICIFSA), Shanghai Jiao Tong University, Shanghai 200240, China*

[4]*Institute of Applied Physics and Computational Mathematics, Beijing 100084, China*

[5]*HEDPS, Center for Applied Physics and Technology, Peking University, Beijing 100871, China*

(Received 5 March 2021; revised 20 May 2021; accepted 1 December 2021; published 14 December 2021)

Theory of absolute stimulated Brillouin side scattering in an inhomogeneous flowing plasma is presented and verified numerically. The linearized coupling equations are transformed into a Schrödinger equation in k space and solved as an eigenvalue problem. Analytic threshold, growth rate, and scattering geometry are obtained for the pump laser with arbitrary incidence angle. Numerical solutions of the coupling equations show good agreements between the theoretical and numerical absolute thresholds when ion-acoustic wave damping is not too large, and thus an old but famous threshold in [Phys. Fluids **17**, 1211 (1974)] is corrected. It also indicates that the theoretical analysis is not accurate for strong dampings, since it will overestimate the absolute threshold. Possibility of finding such instability in the current experiments is also discussed.

DOI: 10.1103/PhysRevE.104.065203

I. INTRODUCTION

Stimulated Brillouin scattering (SBS) and stimulated Raman scattering (SRS) are considered to be significant instabilities in inertial confinement fusion (ICF) for the incident lasers would be scattered by plasma waves. However, after a half century of research, these instabilities are still hard to predict. In addition to the backward scattering, other scattering geometries are becoming more and more significant. Many recent experiments have demonstrated that side scattering cannot be neglected in the context of ICF [1–8]. These side scatterings often result from the laser or plasma asymmetry, such as density inhomogeneity [1,3,9], or multiple overlapping laser beams [6,7,10,11]. Most of these observations are Raman side scatterings, but experimental evidences of Brillouin side scattering have rarely been seen, expect for a few multibeam experiments accomplished decades ago [12–14].

In this paper, we focus on the onset of stimulated Brillouin side scattering caused by the plasma inhomogeneity. It was first realized in the early 1970s that density inhomogeneity can trigger absolute Raman side scattering and flow inhomogeneity can cause absolute Brillouin side scattering. The scattering geometry of absolute Raman side scattering that the wave vector of sidescattered light is nearly perpendicular to the density gradient along which the side scattered light does not feel any density inhomogeneity is well understood. The linear theory of Raman side scattering was first established by Liu, Rosenbluth, and White [15,16], and then Mostrom and Kaufman [17] by solving the Schrödinger equation as an eigenvalue problem in the x space. However, the procedures to obtain absolute threshold are a little bit complicated and require additional assumptions. Another approach to seek absolute instability was first proposed by White *et al.* [18]. They transformed the coupling equations to a Schrödinger equation in k space and solved it by the perturbation method. Compared to resolving the problem in the x space, the latter approach is much easier to apply to multidimensional problems. So, the k-space method is successfully used in obtaining the threshold of absolute two-plasmon decay instability [19,20], as well as absolute stimulated Raman side scattering [21,22].

Compared with flourishing studies on Raman side scattering, there are very few works on the absolute Brillouin side scattering. The first work dated back to the well-known paper of Liu, Rosenbluth, and White [16]. They used two x-space models to solve the coupling equations; one is an envelope model and the other is a full wave model. However, in deriving the threshold of absolute Brillouin side scattering the expression of κ'' (κ is the wave-number mismatch [23]) is incorrect, leading to an incorrect threshold, and the derivation from full wave equations is somewhat ambiguous. Besides, no definite threshold has been concluded and verified. Later Berger [24] retrospected this problem in detail via the envelope model. The absolute threshold they obtained was not explicit and was applied to a situation of local density minimum or maximum, which is not of great interest in the context of ICF. Note that damping of ion acoustic wave under ICF-related parameters is not negligible, the effect of damping on the absolute Brillouin side scattering should be clarified unambiguously.

Therefore, we reconstruct the theory of absolute SBS by transforming the coupling equations into a Schrödinger equation in **k** space, and solve its eigenvalue equation by the perturbation method. Though verified in many other situations, this approach is first used in describing SBS. The threshold, growth rate, and scattering geometry are obtained for the pump laser with arbitrary incidence angle. In order

*xiaocz@hnu.edu.cn

to verify the thresholds, we numerically solve the coupling equations in k space and obtain the convective gain and absolute threshold. The numerical threshold is well consistent with the theoretical threshold when damping is not very large. The previous thresholds derived by Liu *et al.*, which have a different scaling law, have been corrected. We also find that as the damping is getting stronger, the absolute threshold increases, and our analytic threshold with damping terms predicting a higher threshold than the numerical solutions, is not accurate. In addition, this general theory can be readily applied to absolute SRS and gets the same threshold with previous works, validating this powerful method. The renewed understanding of this absolute Brillouin side scattering and analysis of the plasma conditions in current ICF experiments indicate a possibility of finding such instability in the future experiments.

The paper is organized as follows. In Sec. II, we derive the Schrödinger equation in $\mathbf{k}$ space describing SBS in an inhomogeneous flowing plasma with oblique incidence. Then, we solve the eigenvalue equation through a standard perturbation method in Sec. III. Two types of scattering geometries of absolute SBS are shown in Sec. IV. In Sec. V, we mainly focus on discussing the theoretical thresholds with and without damping. Then we present a robust numerical method to solve the coupling equations in k space and compare the theoretical and numerical thresholds in Sec. VI. At last, we summarize our results and discuss the possibility of finding such instability in ICF experiment in Sec. VII.

II. DERIVATION OF SCHRÖDINGER EQUATION IN k SPACE

Stimulated Brillouin scattering strongly relies on flow inhomogeneity, which is often coexistent with plasma density inhomogeneity. But the relationship between these two inhomogeneities is intricate in ICF. For simplicity, linear profiles of plasma density and velocity are assumed here: $n_e(x) = n_0(1 + x/L_n)$ and $\mathbf{V}(x) = -V_0(1 - x/L_V)\hat{\mathbf{x}}$, where L_n, L_V are the density and velocity scale length, respectively, and n_0, V_0 are quantities at resonance, and the pump laser can propagate along an arbitrary direction. The linearized fluid equations of SBS are given by

$$\left(\frac{\partial^2}{\partial t^2} + 2\nu_s\frac{\partial}{\partial t} - c^2\nabla^2 + \omega_p^2\right)\mathbf{a}_s = -\omega_p^2 a_p \mathbf{a}_0, \tag{1}$$

$$\left[\left(\frac{\partial}{\partial t} + \mathbf{V}\cdot\nabla\right)^2 + 2\nu_p\left(\frac{\partial}{\partial t} + \mathbf{V}\cdot\nabla\right) - c_s^2\nabla^2\right]a_p = \frac{Zm_e c^2}{m_i}\nabla^2(\mathbf{a}_0\cdot\mathbf{a}_s), \tag{2}$$

where $\mathbf{a}_0 = e\mathbf{A}_0/m_e c^2 = \frac{1}{2}a_0\hat{\mathbf{e}}_0 e^{i(\mathbf{k}_0\cdot\mathbf{x}-\omega_0 t)} + \text{c.c.}$ and $\mathbf{a}_s = e\mathbf{A}_s/m_e c^2$ are the normalized vector potential of pump and scattered light, respectively, and $a_p = \delta n_i/n_0$ is the normalized density fluctuation of the ion acoustic wave (IAW). $\omega_p^2 = \omega_{p0}^2(1 + x/L_n)$ is the local plasma frequency and $\omega_{p0} = \sqrt{4\pi n_0 e^2/m_e}$ is the plasma frequency at the resonant point, $x = 0$. We also introduce phenomenological damping rates of the scattered light and the ion acoustic wave: $\nu_s = \frac{\omega_p^2}{2\omega_0^2}\nu_{ei}$ and $\nu_p = \nu_{\text{LD}} + \nu_{ei}$, where ν_{ei} is the electron-ion collisional damping rate and ν_{LD} is the Landau damping rate of the ion acoustic wave. Other constants are electron mass (m_e), ion mass (m_i), ion charge state (Z), light velocity (c), and ion sound velocity ($c_s = \sqrt{(ZT_e + T_i)/m_i}$).

By using Fourier transform in space and time,

$$\hat{a}_{s,p}(k,\omega) = \int a_{s,p}(\mathbf{x},t)e^{-i(\mathbf{k}\cdot\mathbf{x}-\omega t)}d\mathbf{x}dt, \tag{3}$$

Eq. (1) reduces to a coupled equation for the scattered light,

$$i\frac{\omega_{p0}^2}{L_n}\frac{\partial\hat{a}_s}{\partial k_x} + D_l\hat{a}_s = -\frac{1}{2}\omega_{p0}^2 a_0(\hat{a}_{p+} + \hat{a}_{p-}), \tag{4}$$

where $D_l = -\omega^2 + \omega_{p0}^2 + k^2c^2 - 2i\omega\nu_s$ is the light wave dispersion function. And Eq. (2) is simplified as

$$\frac{k_x^2V_0^2}{L_V^2}\frac{\partial^2\hat{a}_p}{\partial k_x^2} + \left[3k_x\frac{V_0^2}{L_V^2} + 2i\frac{k_xV_0}{L_V}(\omega + k_xV_0 + i\nu_p)\right]\frac{\partial\hat{a}_p}{\partial k_x} + \left[D_p + \frac{V_0^2}{L_V^2} + i\frac{V_0}{L_V}(2\omega + 3k_xV_0 + 2i\nu_p)\right]\hat{a}_p = -\frac{Zm_ec^2a_0k^2}{2m_i}(\hat{a}_{s-} + \hat{a}_{s+}), \tag{5}$$

where $D_p = -(\omega + k_xV_0)^2 + k^2c_s^2 - 2i(\omega + k_xV_0)\nu_p$ is the IAW dispersion function. The subscript "+" and "−" represent $(\mathbf{k} + \mathbf{k}_0, \omega + \omega_0)$ and $(\mathbf{k} - \mathbf{k}_0, \omega - \omega_0)$, respectively.

The partial differential, $(\partial/\partial k_x)^n$, stems from the Fourier transform of x^n. The inhomogeneous term $\omega_p^2 = \omega_{p0}^2(1 + x/L_n)$ contributes to $\partial/\partial k_x$ in Eq. (4), while an x^2-inhomogeneity from $(\partial/\partial t + \mathbf{V}\cdot\nabla)^2$ leads to $\partial^2/\partial k_x^2$ in Eq. (5). To proceed, we neglect the second-order derivation since $kL_V \gg 1$ and keep only the lowest order of $1/kL_V$ in each term; then Eq. (4) and Eq. (5) can be simplified as

$$i\mathscr{L}_s\frac{\partial\hat{a}_s}{\partial k_x} + D_l\hat{a}_s = -\frac{1}{2}\omega_{p0}^2 a_0(\hat{a}_{p+} + \hat{a}_{p-}), \tag{6}$$

$$i\mathscr{L}_p\frac{\partial\hat{a}_p}{\partial k_x} + D_p\hat{a}_p = -\frac{Zm_ec^2a_0k^2}{2m_i}(\hat{a}_{s-} + \hat{a}_{s+}), \tag{7}$$

where $\mathscr{L}_s = \omega_{p0}^2/L_n$ and $\mathscr{L}_p = 2k_xV_0(\omega + k_xV_0)/L_V$. Combining these two equations and eliminating $\hat{a}_p$, we have a second-order ordinary differential equation (ODE),

$$\frac{\partial^2\hat{a}_{s-}}{\partial k_x^2} - i\left(\frac{D_{l-}}{\mathscr{L}_s} + \frac{D_p}{\mathscr{L}_p}\right)\frac{\partial\hat{a}_{s-}}{\partial k_x} + \left(\frac{\Gamma^2 - D_pD_{l-}}{\mathscr{L}_s\mathscr{L}_p} - i\frac{1}{\mathscr{L}_s}\frac{\partial D_{l-}}{\partial k_x}\right)\hat{a}_{s-} = 0, \tag{8}$$

where $\Gamma^2 = k^2a_0^2c^2\omega_{pi}^2/4$. Equation (8) can reduce to the standard form of Schrödinger equation just by introducing

$$\hat{a}_{s-}(k_x,\omega) = W(k_x,\omega)e^{\frac{i}{2}\int(\frac{D_{l-}}{\mathscr{L}_s} + \frac{D_p}{\mathscr{L}_p})dk_x}, \tag{9}$$

and thus the Schrödinger equation in k space is

$$\frac{\partial^2 W}{\partial k_x^2} + F(k_x,\omega)W = 0. \tag{10}$$

We sort the potential in descending powers of L_n and L_V: $F = F_0 + F_1$, and

$$F_0 = \frac{1}{4}\left(\frac{D_{l-}}{\mathscr{L}_s} - \frac{D_p}{\mathscr{L}_p}\right)^2 + \frac{\Gamma^2}{\mathscr{L}_s\mathscr{L}_p}, \tag{11}$$

$$F_1 = \frac{i}{2}\frac{\partial}{\partial k_x}\left(\frac{D_{l-}}{\mathscr{L}_s} - \frac{D_p}{\mathscr{L}_p}\right). \tag{12}$$

L_V and L_n are often in the same order.

Equations (10)–(12) form a second-order ODE in k space describing SBS in a plasma of linear inhomogeneity. These equations have the same forms with those derived in Ref. [21] for absolute Raman side scattering, but the formulas are much more complicated due to the flow inhomogeneity. The potential $F(k_x, \omega)$ is a complicated function of k_x. We can solve the Schrödinger equation by the WKB method when $F(k_x, \omega) \neq 0$, and the approximated solution is given by $W_\pm \approx W_0 F^{-1/4} \exp(\pm i \int \sqrt{F} dk_x)$ [25]. The phase integral gives us a finite gain, which is definitely the Rosenbluth gain, $G = \pi\gamma_0^2/\kappa' V_{sx} V_{px}$ [23], when damping is negligible. However, the WKB method is no longer valid as $F(k_x, \omega)$ approaches zero. Then Eq. (10) must be solved through the eigenvalue problem, and the imaginary part of eigenvalues implies an absolute instability may exist. Here, absolute Brillouin scatterings may occur when $F(k_x, \omega) \approx 0$, which indicates that the scattering geometry should satisfy,

$$\frac{\partial}{\partial k_x}\left(\frac{D_{l-}}{\mathscr{L}_s} - \frac{D_p}{\mathscr{L}_p}\right) = 0. \tag{13}$$

In Sec. IV, we will discuss the condition in detail, but before that we solve the eigenvalue equation of this Schrödinger equation to obtain the growth rate and threshold via a standard procedure verified by many authors [19–22].

III. EIGENVALUE SOLUTION OF SCHRÖDINGER EQUATION

To solve the Schödinger equation when $F(k_x, \omega) = 0$, the joining condition, also known as the Bohr-Sommerfeld quantization condition, should be satisfied,

$$\int_{k_1}^{k_2} \sqrt{F(k_x, \omega)} dk_x = \left(n + \frac{1}{2}\right)\pi, \tag{14}$$

where k_1 and k_2 are the turning points of the potential well, satisfying $F(k_x, \omega) = 0$. Since the potential is much more complicated, we use the perturbation method to find the eigenvalue. As is well known, the density and velocity scale lengths in ICF conditions is approximately hundreds of microns, or even millimeters, so we have $kL_n \gg 1$ and $kL_V \gg 1$. Absolute instability can exist in such condition when the WKB approximation violates. To find the eigenmodes, first we apply Eq. (14) to the homogeneous case, i.e., $(L_n, L_V) \to \infty$, so F_0 dominates the potential, and k_1 and k_2 must merge to have a finite integral. This gives us the equations to find the homogeneous growth rate,

$$F_0(k_x, \omega) = \frac{\partial F_0(k_x, \omega)}{\partial k_x} = 0. \tag{15}$$

In deriving the homogeneous growth rate, we assume $\omega = \omega_r + i\gamma$, and ω_r satisfies the dispersion relation of the ion acoustic wave: $\omega_r = kc_s - k_x V_0$. In the weak coupling limit ($\gamma \ll \omega_r$), the dispersion functions is reduced as $D_p \approx -2ikc_s(\gamma + \nu_p)$ and $D_{l-} \approx 2i\omega_0(\gamma + \nu_s)$. Substituting Eq. (11) into Eq. (15), we can readily obtain the homogeneous growth rate,

$$\gamma_h = \gamma_0 - \bar{\nu}, \tag{16}$$

where

$$\gamma_0 = \sqrt{\frac{\Gamma^2}{4\omega_0 kc_s}} \times \frac{\sqrt{4(\omega_0/\mathscr{L}_s)(kc_s/\mathscr{L}_p)}}{\omega_0/\mathscr{L}_s + kc_s/\mathscr{L}_p}, \tag{17}$$

$$\bar{\nu} = \frac{\omega_0/\mathscr{L}_s}{\omega_0/\mathscr{L}_s + kc_s/\mathscr{L}_p}\nu_s + \frac{kc_s/\mathscr{L}_p}{\omega_0/\mathscr{L}_s + kc_s/\mathscr{L}_p}\nu_p. \tag{18}$$

$\gamma_B \equiv \sqrt{\frac{\Gamma^2}{4\omega_0 kc_s}} = kv_0\omega_{pi}/4\sqrt{kc_s\omega_0}$ is the SBS growth rate in homogenous plasma.

Next we deal with the weak inhomogeneous plasma. Potential F is a finite function and also dominated by F_0, since $kL_n, kL_V \gg 1$. Then we can expand $F(k_x, \gamma)$ in a Taylor series near the homogeneous state (k_h, γ_h),

$$F \approx F_0\big|_{k_h,\gamma_h} + \frac{\partial F_0}{\partial k_x}\bigg|_{k_h,\gamma_h}(k_x - k_h) + \frac{1}{2}\frac{\partial^2 F_0}{\partial k_x^2}\bigg|_{k_h,\gamma_h}(k - k_h)^2 + \frac{\partial F_0}{\partial \gamma}\bigg|_{k_h,\gamma_h}(\gamma - \gamma_h) + F_1\big|_{k_h,\gamma_h}. \tag{19}$$

The first two terms vanish, and to keep the lowest order, we neglect the last term. Thus, by substituting Eq. (19) into the eigenvalue equation [Eq. (14)], we have the growth rate in the inhomogeneous plasma,

$$\gamma = \gamma_h + \left(n + \frac{1}{2}\right)\frac{(-2\partial^2 F_0/\partial k_x^2)^{1/2}\big|_{k_h,\gamma_h}}{\partial F_0/\partial\gamma\big|_{k_h,\gamma_h}}. \tag{20}$$

The quantities $\partial^2 F_0/\partial k_x^2$ and $\partial F_0/\partial\gamma$ are easily obtained from Eq. (11) and Eq. (15),

$$\frac{\partial^2 F_0}{\partial k_x^2} \approx \frac{1}{2}\left(\frac{D_{l-}}{\mathscr{L}_s} - \frac{D_p}{\mathscr{L}_p}\right)\frac{\partial^2}{\partial k_x^2}\left(\frac{D_{l-}}{\mathscr{L}_s} - \frac{D_p}{\mathscr{L}_p}\right), \tag{21}$$

$$\frac{\partial F_0}{\partial \gamma} = i\left(\frac{D_{l-}}{\mathscr{L}_s} - \frac{D_p}{\mathscr{L}_p}\right)\left(\frac{\omega_0}{\mathscr{L}_s} + \frac{kc_s}{\mathscr{L}_p}\right). \tag{22}$$

One should note that $\frac{\partial^2}{\partial k_x^2}(\frac{D_{l-}}{\mathscr{L}_s}) = 2c^2/\mathscr{L}_s \gg \frac{\partial^2}{\partial k_x^2}(\frac{D_p}{\mathscr{L}_p})$, so we neglect the corresponding term in Eq. (21). Substituting the two formulas into Eq. (20) and using Eqs. (15) and (17), we finally obtain the eigenvalues,

$$\gamma = \gamma_0\left[1 + (i-1)\frac{(n+\frac{1}{2})\sqrt{c^2/\mathscr{L}_s}}{\sqrt{2}(\frac{\Gamma^2}{\mathscr{L}_s\mathscr{L}_p})^{3/4}}\right] - \bar{\nu}. \tag{23}$$

The real part of γ is the inhomogeneous growth rate,

$$\mathrm{Re}[\gamma] = \gamma_0\left[1 - \frac{(n+\frac{1}{2})\sqrt{c^2/\mathscr{L}_s}}{\sqrt{2}(\frac{\Gamma^2}{\mathscr{L}_s\mathscr{L}_p})^{3/4}}\right] - \bar{\nu}. \tag{24}$$

The effect of plasma inhomogeneity demonstrated by the second term in the bracket implies both density and velocity inhomogeneity play roles as effective dampings on the growth rate, and the real damping terms obviously decrease

the growth rate. If damping is negligible, the threshold to the lowest order ($n = 0$) is

$$\frac{4\Gamma^2}{\mathscr{L}_s\mathscr{L}_p} > \left(\frac{c^2}{\mathscr{L}_s}\right)^{2/3}. \tag{25}$$

Substituting Γ^2, $\mathscr{L}_s$, and $\mathscr{L}_p$ mentioned above, we obtain the threshold for absolute Brillouin scattering,

$$\left(\frac{v_0}{v_e}\right)^2\left(\frac{\omega_0}{c}L_V\right)^{4/3} > 2M_a\left(\frac{\omega_0}{\omega_{p0}}\right)^{4/3}\left(\frac{L_V}{L_n}\right)^{1/3}\left(\frac{k_x}{k}\right), \tag{26}$$

where $M_a = V_0/c_s$ is the Mach number at the resonant point, $v_0 = a_0 c$ is the quiver velocity, and $v_e = \sqrt{T_e/m_e}$ is the electron thermal velocity.

The existence of such absolute instability requires that the Bohr-Sommerfeld quantization condition be valid, which means the interaction length in the k space must be larger than $\Delta k = \mathrm{Re}(\mathrm{k}_1 - \mathrm{k}_2)$. Therefore, the localized region of absolute instability has a width (for the lowest order $n = 0$),

$$\Delta k \approx 2.4M_a^{1/8}\left(\frac{v_e}{v_0}\right)^{1/4}\left(\frac{\omega_{p0}}{\omega_0}\right)^{1/2}\left(\frac{k_x L_n}{kL_V}\right)^{1/8}\left(\frac{\omega_0}{L_n c}\right)^{1/2}. \tag{27}$$

The damping-free threshold is checked by numerical solutions of coupling equations in k space in Sec. VI. When compared to previous results [$(v_0^2/v_e^2)(k_0L_V)^{4/3} > \beta L_V/L_n$ in Ref. [16] where β is some constant], the scaling law is different. This difference is due to incorrect $\kappa'' = -2k/L_V^2$ (where κ is the wave-number mismatch) used in their paper, while if a correct κ'' is derived, we can obtain the same scalings with Eq. (26). In addition, our results can also be verified by absolute Raman scattering. If we replace $\Gamma^2 = k^2a_0^2c^2\omega_{pe}^2/4$ and $\mathscr{L}_s = \mathscr{L}_p = \omega_{p0}^2/L_n$, which are readily obtained from coupling equations of Raman scattering, one can recover the damping-free threshold of absolute Raman scattering [21] by evaluating Eq. (25).

IV. GEOMETRY OF ABSOLUTE BRILLOUIN SCATTERINGS

Absolute Brillouin scattering occurs when Eq. (13) is satisfied. We assume in a local plasma the incidence angle to the x axis is θ, so it is readily obtained that $\partial D_{l-}/\partial k_x = 2c^2(k_x - k_0\cos\theta)$ and $\frac{\partial}{\partial k_x}\left(\frac{D_p}{2k_xV_0(\omega+k_xV_0)}\right) \approx \frac{1}{M_a|k|} - \frac{1}{k_x}$. Equation (13) reduces to

$$\frac{2L_nc^2(k_x - k_0\cos\theta)}{\omega_{p0}^2} = L_V\left(\frac{1}{M_a|k|} - \frac{1}{k_x}\right). \tag{28}$$

The equation is solved according to a specific resonant condition. For oblique incidence, different polarizations have different resonant conditions, since the polarization direction of scattered light shall be parallel to that of the pump laser to keep a maximum ponderomotive force.

Therefore, we discuss two types of polarizations in this paper: The incident laser is s polarized where its electric field is perpendicular to the plane of $\hat{\mathbf{x}}$ and $\mathbf{k}_0$, and p polarized where the electric field is in that plane. The general resonant conditions of s- and p-polarized SBS are shown in Figs. 1(a) and 1(b), respectively, and we assume the scattering angle to the x axis is φ. First for an s-polarized laser, we readily obtain

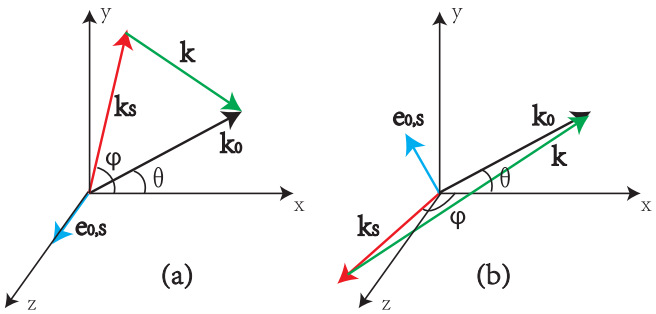

FIG. 1. General Brillouin scattering geometries of (a) an s-polarized laser and (b) a p-polarized laser. The x axis is the direction of the density and velocity gradients, and the propagation direction of pump and scattered lights are θ and ϕ to the x axis, respectively.

the wave vectors of each decay wave from the three-wave matching condition,

$$|k_s| \approx |k_0|,\ |k| \approx 2|k_0|\sin\left(\frac{\varphi - \theta}{2}\right),$$
$$k_x \approx |k_0|(\cos\theta - \cos\varphi). \tag{29}$$

Substituting Eq. (29) into Eq. (28), we have

$$\frac{(\cos\theta - \cos\varphi)\cos\varphi}{1 - \sin(\frac{\theta+\varphi}{2})/M_a} = \frac{\omega_{p0}^2}{2k_0^2c^2}\frac{L_V}{L_n}. \tag{30}$$

Solving for φ, we obtain the scattering geometry of absolute Brillouin scattering with an s-polarized laser. While for a p-polarized laser, the corresponding wave vectors in Fig. 1(b) are

$$|k_s| \approx |k_0|,\ |k| \approx |k_0|\sqrt{2 - 2\frac{\cos\varphi}{\cos\theta}},\ k_x \approx |k_0|(\cos\theta - \cos\varphi). \tag{31}$$

Also substituting into Eq. (28), we have the scattering geometry of a p-polarized pump laser,

$$\frac{(\cos\theta - \cos\varphi)\cos\varphi}{1 - \frac{1}{M_a}\sqrt{\frac{1}{2}(\cos\theta - \cos\varphi)\cos\theta}} = \frac{\omega_{p0}^2}{2k_0^2c^2}\frac{L_V}{L_n}. \tag{32}$$

The solutions of Eqs. (30) and (32) are shown in Fig. 2 for $M_a = 1.5$ and different $\alpha \equiv (\omega_{p0}^2/2k_0^2c^2)(L_V/L_n)$. There exist two types of absolute Brillouin scattering geometries: k_{sx} or k_x approaches to zero. If $\alpha \ll 1$, φ approaches 90° or 270°, which makes $k_{sx} \approx 0$, i.e., the scattered light is perpendicular to the velocity gradient. The other solution is φ approaches θ or $360° - \theta$, which makes k_x vanish. $\varphi \approx \theta$ means the scattering is fully forward and $\varphi \approx 360° - \theta$ also indicates a forward scattering. These situations are depicted by black and blue curves in Fig. 2. As α increases, the region of absolute instability shrinks. For $M_a \gg 1$, no absolute SBS could occur when $\alpha > \cos^2\theta/4$, which implies that the absolute SBS is prohibited at high densities. As M_a decreases, one would expect a larger region of absolute instability. We also find that there is no big difference between the scattering geometries of an s-polarized pump and a p-polarized pump.

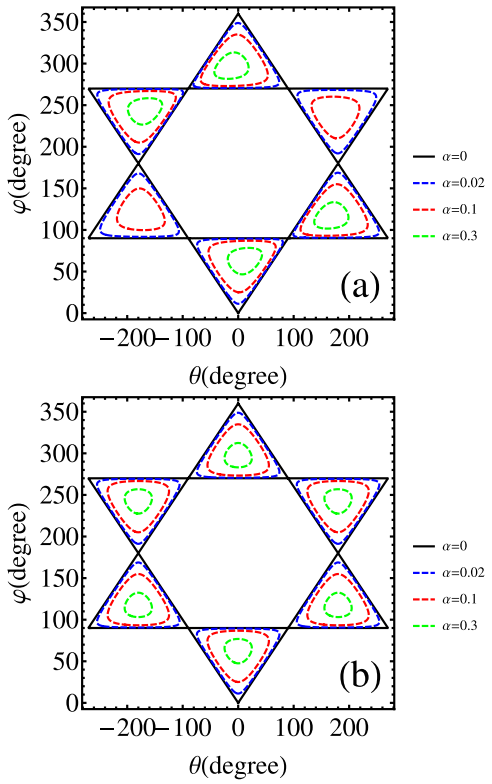

FIG. 2. Solutions of (a) Eq. (30) and (b) Eq. (32) with $M_a = 1.5$ and $\alpha \equiv (\omega_{p0}^2/2k_0^2c^2)(L_V/L_n) = 0, 0.02, 0.1$ and 0.3.

V. THRESHOLD FOR ABSOLUTE BRILLOUIN SIDE SCATTERING

Among two absolute scattering geometries, we are interested in the absolute Brillouin side scattering where $\varphi \approx 90^\circ$ or 270°, since the absolute forward Brillouin scattering has an infinitesimal growth rate, $\gamma_0 \to 0$ as $k_x \to 0$. Also, there are three types of absolute Brillouin side scatterings: two s-polarized lasers with $\varphi \approx 90^\circ$ and $\varphi \approx 270^\circ$, which are, respectively, the forward and backward side scatterings, and one p-polarized laser with $\varphi \approx 90^\circ$ or $\varphi \approx 270^\circ$ (these two modes are the same).

Substituting the scattering geometries discussed in Sec. IV into the threshold formulas, we can obtain the theoretical intensity thresholds. In Fig. 3, we plot dependencies of intensity thresholds on four quantities with three types of Brillouin side scatterings. Collisional and Landau dampings are neglected here, so the threshold is determined by Eq. (26). The black-solid, red-dashed, and green-dash-dotted curves represent the forward side scattering of the s-polarized pump, backward side scattering of the s-polarized pump, and side scattering of the p-polarized pump, respectively. Unless the variable is discussed, the parameters are $\lambda_0 = 351\ \mu$m, $L_V/L_n = 1$, $T_e = 1$ keV, $L_V = 200\ \mu$m, $M_a = 1.5$, $n_e = 0.1n_c$, and $\theta = 30^\circ$.

As shown, backward side scattering has the lowest threshold, and then comes the p-polarized and forward side scatterings subsequently, in accordance with the descending IAW wave number. Figure 3(a) shows the velocity scale length dependence of the intensity threshold, which is relatively low when damping is neglected. It has a scaling law of $I_{\text{threshold}} \propto L_V^{-4/3}$. In Fig. 3(b), as the Mach number increases, the threshold increases almost linearly, so $I_{\text{threshold}} \propto M_a$.

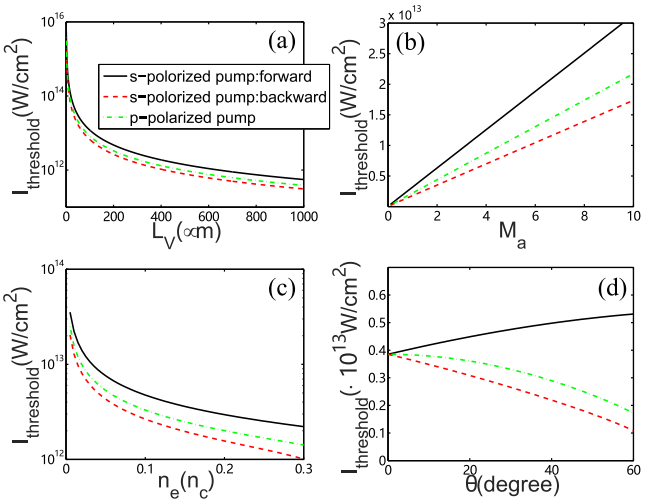

FIG. 3. (a)–(d) The dependencies of velocity scale length, Mach number, electron density, and incidence angle on the intensity thresholds, respectively. Thresholds of three types of absolute Brillouin side scatterings are compared. Unless the variable is discussed, the parameters are $\lambda_0 = 351\ \mu$m, $L_V/L_n = 1$, $T_e = 1$ keV, $L_V = 200\ \mu$m, $M_a = 1.5$, $n_e = 0.1n_c$, and $\theta = 30^\circ$.

The plasma density not only acts as a scaling term on the right-hand side of Eq. (26), but also strongly affects the scattering geometry. Figure 4(a) shows the scattering

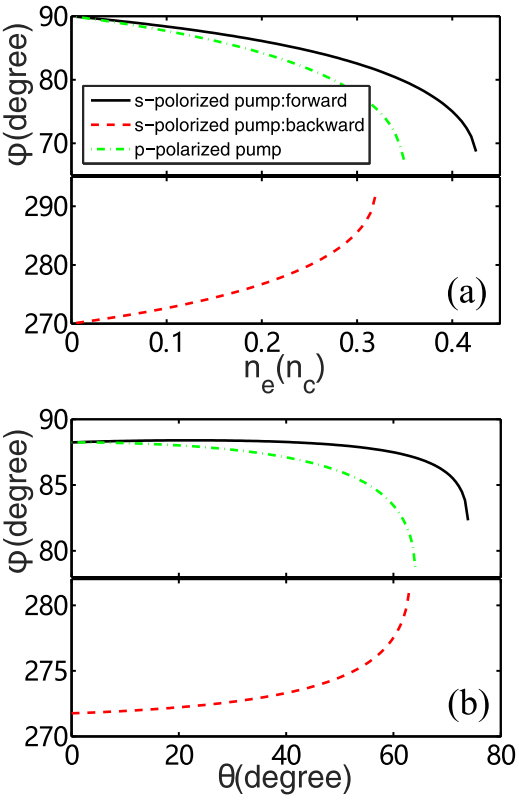

FIG. 4. The corresponding scattering angles of (a) Fig. 3(c), and (b) Fig. 3(d).

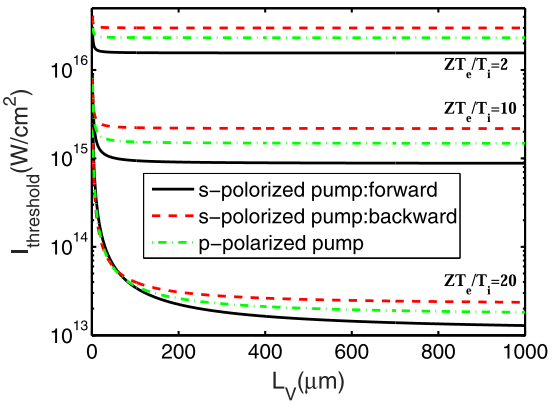

FIG. 5. Intensity threshold with the effect of Landau damping, obtained by solving $\mathrm{Re}[\gamma] = 0$. Three different electron-to-ion temperatures with $Z = 1$ are discussed, and other parameters are the same with Fig. 3(a).

angle of side-scattered lights as a function of plasma density. When plasma density increases, the side-scattered light slowly changes its propagation direction from the perpendicular direction towards the x axis. However, the backward, p-polarized, and forward side scatterings are quenched at $n_e = 0.32, 0.35,$ and $0.425 n_c$, respectively. Below those densities, the intensity threshold decreases as the density increases and satisfies a scaling law of $I_{\mathrm{threshold}} \propto n_e^{-2/3}$ as long as it is not too close to the quenching point as shown in Fig. 3(c).

The θ dependence of the intensity threshold is a little complicated. It is involved in the threshold condition through the geometry term, k_x/k. As shown in Fig. 4(b), the scattering angles are slowly changed until they reach the quenching points, which are 64°, 65°, and 74° for the corresponding scattering geometry. The intensity threshold shows different behaviors for different side scatterings. For forward side scattering, the intensity threshold increases with the incidence angle, while it has an opposite trend for the other two side scatterings. But we observe that these variations are not remarkable, which means the threshold is weakly dependent on the incidence angle.

The theoretical thresholds considering the effect of damping are also discussed. As is well known, the Landau damping of the ion acoustic wave mostly depends on ZT_e/T_i, and collisional damping is negligible in the interested parameter space. We numerically solve the threshold equation, $\mathrm{Re}[\gamma] = 0$, and plot the velocity scale length dependence of the intensity threshold in Fig. 5 under the same conditions as Fig. 3(a) and H^+ ions ($Z = 1$). As the ion temperature increases from zero [Fig. 3(a)] to $0.5T_e$, the Landau dampings of IAW waves are $\nu_p/kc_s = 0.017, 0.15,$ and 0.45 for $ZT_e/T_i = 20, 10,$ and 2, respectively, which corresponds to ICF relevant situations from weak to strong Landau damping. Under weak Landau damping, the intensity threshold still remains at a low level. Absolute Brillouin side scattering could occur there. As the ion temperature increases to the level of electron temperature, strong Landau damping lifts the absolute threshold dramatically. However, this is not the whole picture, since with strong damping the theoretical analysis is not accurate enough to give a correct threshold, which will be shown in numerical results in the next section. Even though one should also note that the sort from the lowest threshold to the highest threshold is reversed. The forward side scattering of the s-polarized pump has the lowest intensity threshold because of its smallest IAW wave number, leading to the smallest Landau damping. This would make the forward side scattering easier to occur when damping is included.

VI. NUMERICAL SOLUTIONS, CONVECTIVE GAIN, AND COMPARISON WITH THEORETICAL THRESHOLDS

Numerical solutions of coupling equations in k space are performed to verify the theoretical threshold of absolute stimulated Brillouin side scattering. Instead of numerically seeking for the eigenmodes of the complex Schrödinger equation [Eq. (10)] through the WKB numerical method or shooting method [20], here we employ a method integrating the coupling equations to find the convective gain and absolute threshold. This method has recently been used to study stimulated Raman side scattering [3,22].

Before numerical integrating the coupling equations in the k space, we introduce a transform $\hat{a}_s(k_x) = A_s(k_x)\exp[i\int(D_l/\mathscr{L}_s)dk_x]$ and $\hat{a}_{p-}(k_x) = A_p(k_x)\exp[i\int(D_{p-}/\mathscr{L}_{p-})dk_x]$, so Eqs. (6) and (7) are simplified as

$$\frac{\partial A_s}{\partial k_x} = i\frac{\omega_{p0}^2 a_0}{2\mathscr{L}_s}A_p e^{i\int(\frac{D_{p-}}{\mathscr{L}_{p-}}-\frac{D_s}{\mathscr{L}_s})dk_x}, \tag{33}$$

$$\frac{\partial A_p}{\partial k_x} = i\frac{Zm_e c^2 a_0 k_-^2}{2m_i\mathscr{L}_{p-}}A_s e^{-i\int(\frac{D_{p-}}{\mathscr{L}_{p-}}-\frac{D_s}{\mathscr{L}_s})dk_x}, \tag{34}$$

where A_s and A_p are nonoscillated quantities, leading to a better numerical stability.

The numerical integral starts from the vacuum $k_{\mathrm{out}} = -\sqrt{(\omega_s/c)^2 - k_{sy}^2}$, via the resonant point $k_x = 0$, and reflects back to the vacuum $k_{\mathrm{in}} = \sqrt{(\omega_s/c)^2 - k_{sy}^2}$ (i.e., an integral length of $2L_n$ in real space), where ω_s and k_{sy} are the frequency and transverse wave number of the sidescattered light, respectively. The outgoing wave boundary conditions are used: $A_s(k_{\mathrm{out}}) = 1$ and $A_p(k_{\mathrm{out}}) = 0$. Collisional damping is not considered here, so $|A_s|$ only decreases near the resonant point and gets a stable amplitude at $k_x = k_{in}$. The gain of side-scattered light can be defined by $G = \log(|\hat{a}_s(k_{\mathrm{out}})|^2/|\hat{a}_s(k_{\mathrm{in}})|^2)$, and it is sensitive to the scattered wave number. Assuming a fixed frequency and change k near the resonant point, we can obtain a maximum gain right at the real part of the eigenvalue in the k space [26]. In addition, a local maximum gain is expected when the imaginary part of the eigenvalue vanishes, which is exactly the absolute threshold.

For example, Fig. 6 shows the gain as a function of incident laser intensity in two different situations: (a) without damping, and (b) with strong damping. When damping is negligible, an obvious peak is observed. This peak corresponds to the state of the vanishing imaginary part of the eigenvalue, therefore, it is the absolute threshold. Below that intensity, only convective instability occurs, characterized by the convective gain, while above that intensity, absolute instability occurs and the gain becomes meaningless. As damping increases, the absolute threshold increases along with an increase of gain in the absolute unstable region, making the observation of resonant peak

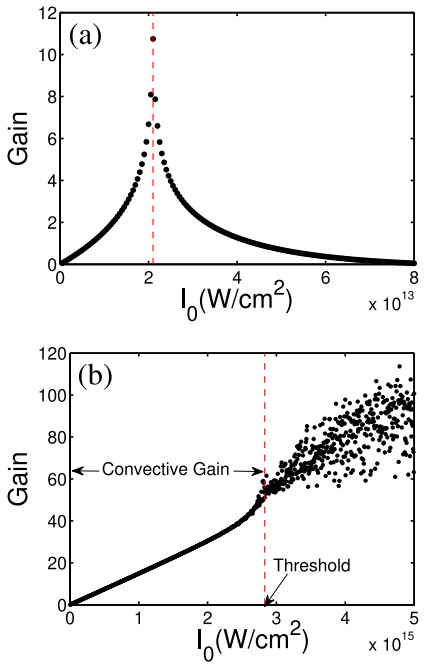

FIG. 6. Gain evaluated from $G = \log(|\hat{a}_s(k_{\rm out})|^2/|\hat{a}_s(k_{\rm in})|^2)$ as a function of incident laser intensity. (a) Case without damping, $T_e = 1$ keV, $L_V = L_n = 50$ μm, $M_a = 1.5$, $n_e = 0.1n_c$, and $\theta = 0^\circ$. (b) Case with strong damping, $ZT_e/T_i = 2$, $L_V = L_n = 100$ μm, and other parameters are the same with (a). Red dashed line denotes the absolute threshold.

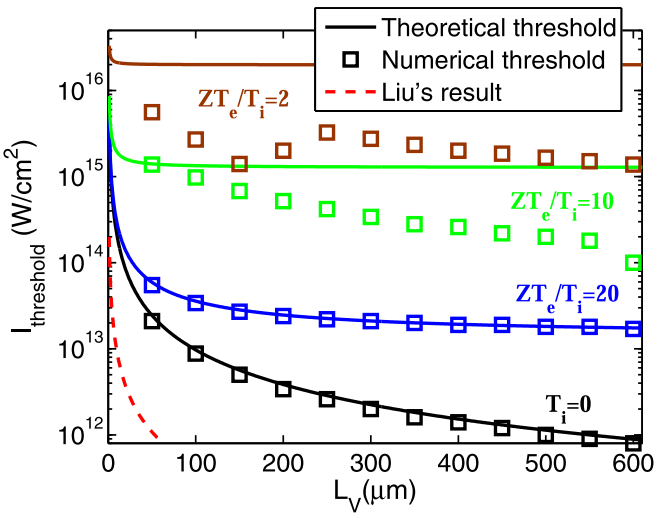

FIG. 7. Comparison of theoretical (solid lines), numerical threshold (squares), and Liu's result [(dashed line) Eq. (65a) in Ref. [16]]. Four different dampings of $ZT_e/T_i = 2, 10, 20, \infty$ are plotted. All cases are normal incidence $\theta = 0^\circ$, and other parameters are the same as Fig. 3(a).

difficult. An extreme case is shown in Fig. 6(b) where strong Landau damping at $ZT_e/T_i = 2$ is set and no peak is found here. The absolute threshold is a line separating the regular and chaotic behavior, and beneath the absolute threshold we see a linear increasing of the convective gain. Although the absolute threshold is as high as $10^{15}W/\text{cm}^2$, the convective gain is also high enough making the convective side scattering remarkable.

With this method, we can find the absolute threshold numerically and compare with our theoretical threshold. Here, we compare the previous threshold [Eq. (65a) in Ref. [16]] with our theoretical and numerical thresholds in Fig. 7. Since Liu *et al.* only considered normal incidence and no dampings are included, we assume normal incidence $\theta = 0^\circ$ in Fig. 7. Our theoretical and numerical thresholds without damping ($T_i = 0$) are well consistent and it is far beyond the Liu's result. Their threshold has the same scaling of I_0 and L_n as ours $[(v_0/v_e)^2(k_0L_n)^{4/3} \approx 0.48]$, but its coefficient in the right-hand side is too small and irrelevant with the Mach number and density, which seems incorrect intuitively. As damping is included, theoretical threshold and numerical thresholds begin to separate when $ZT_e/T_i \lesssim 10$. The numerical thresholds are lower than the theoretical thresholds, which may give us the possibility to observe absolute Brillouin side scattering at the high ion-acoustic-wave damping regime.

Therefore, our damping-free threshold, Eqs. (26) or (25), is verified by the numerical results, however, the theoretical threshold with damping [$\text{Re}[\gamma] = 0$, evaluated from Eq. (24)] is accurate only when the damping is small. This discrepancy may come from the perturbation method of finding eigenmodes, since we find the same problem when comparing numerical and theoretical thresholds of absolute Raman side scattering using Afeyan's results [21].

VII. CONCLUSIONS AND DISCUSSIONS

The theory of absolute stimulated Brillouin scattering in an inhomogeneous flowing plasma is presented. Different from the previous studies of absolute SBS [16,24], here we transform the coupling equations to a Schrödinger equation in the k space, and solve the Schrödinger equation as an eigenvalue problem by the perturbation method. This approach has been successfully used to derive the threshold of absolute Raman side scattering and two-plasmon decay, but is first used for SBS. There are two types of absolute Brillouin scatterings: the forward scattering and side scattering. Among them, side scattering is of great importance since the growth rate of forward scattering almost vanishes. The theoretical threshold and growth rate that we obtained have corrected Liu's result of absolute Brillouin side scattering, and extended to the case of the arbitrary incidence angle and with the effect of damping considered. Numerical solutions of the coupling equations in the k space show us good agreement between the theoretical and numerical thresholds when damping is not significantly large, however, the theory overestimates the threshold when $ZT_e/T_i \lesssim 10$ where strong Landau damping with $\nu_p \gtrsim 0.1kc_s$ is seen.

In the context of ICF, Brillouin side scattering has not been observed yet. There still are possibilities to find such instability, since the velocity scale length is as long as several hundred of microns, or even millimeters (in the indirect-drive scheme), the Mach number is on the order of unity, and the threshold is not very sensitive to the incidence angles. The absolute threshold under such conditions and without damping is as low as $10^{13}W/\text{cm}^2$. The only concern is the Landau damping of IAW, which strongly relies on ZT_e/T_i. Usually, $T_e \geqslant T_i$ and

Z is determined by the materials. A high Z environment is often seen in the Au wall of the indirect-drive ICF, and the middle Z environment is used in doped ablation material in the direct-drive scheme [27]. Even so, in the environment of low Z materials such as H, He, Be, C, etc., the Brillouin side scattering may still have a chance to occur in the convective regime [as depicted in Fig. 7(b)], unexpected hot-spot speckles [28], nonlinear regimes that eliminate the Landau dampings [29–31], or new ignition schemes with higher laser intensity [32–35]. What makes this side scattering an invisible phenomenon is perhaps the shortage of measured equipment. For example, the forward side scattering has a lower Landau damping, thus a lower threshold, and it may occur more easily, but the trajectory of this scattering is not pointed to the detectors, making the observation difficult. Therefore, stimulated Brillouin side scattering is a possible instability in ICF, but its existence is yet to be seen, experimentally.

ACKNOWLEDGMENTS

This work was supported by the Strategic Priority Research Program of Chinese Academy of Sciences (Grant No. XDA25050700), National Natural Science Foundation of China (Grants No. 11805062 and No. 11774430), Science Challenge Project (Project No. TZ2016005), and Natural Science Foundation of Hunan Province, China (Grant No. 2020JJ5029).

[1] M. J. Rosenberg, A. A. Solodov, W. Seka, R. K. Follett, J. F. Myatt, A. V. Maximov, C. Ren, S. Cao, P. Michel, M. Hohenberger *et al.*, Phys. Plasmas **27**, 042705 (2020).
[2] S. Depierreux, C. Neuville, V. Tassin, M.-C. Monteil, P.-E. Masson-Laborde, C. Baccou, P. Fremerye, F. Philippe, P. Seytor, D. Teychenné *et al.*, Plasma Phys. Controlled Fusion **62**, 014024 (2020).
[3] P. Michel, M. J. Rosenberg, W. Seka, A. A. Solodov, R. W. Short, T. Chapman, C. Goyon, N. Lemos, M. Hohenberger, J. D. Moody, S. P. Regan, and J. F. Myatt, Phys. Rev. E **99**, 033203 (2019).
[4] G. Cristoforetti, L. Antonelli, D. Mancelli, S. Atzeni, F. Baffigi, F. Barbato, D. Batani, G. Boutoux, F. D'Amato, J. Dostal *et al.*, High Power Laser Sci. Eng. **7**, 0300e51 (2019).
[5] M. J. Rosenberg, A. A. Solodov, J. F. Myatt, W. Seka, P. Michel, M. Hohenberger, R. W. Short, R. Epstein, S. P. Regan, E. M. Campbell, T. Chapman, C. Goyon, J. E. Ralph, M. A. Barrios, J. D. Moody, and J. W. Bates, Phys. Rev. Lett. **120**, 055001 (2018).
[6] S. Depierreux, C. Neuville, C. Baccou, V. Tassin, M. Casanova, P. E. Masson-Laborde, N. Borisenko, A. Orekhov, A. Colaitis, A. Debayle, G. Duchateau, A. Heron, S. Huller, P. Loiseau, P. Nicolai, D. Pesme, C. Riconda, G. Tran, R. Bahr, J. Katz, C. Stoeckl, W. Seka, V. Tikhonchuk, and C. Labaune, Phys. Rev. Lett. **117**, 235002 (2016).
[7] P. Michel, L. Divol, E. L. Dewald, J. L. Milovich, M. Hohenberger, O. S. Jones, L. B. Hopkins, R. L. Berger, W. L. Kruer, and J. D. Moody, Phys. Rev. Lett. **115**, 055003 (2015).
[8] C. Neuville, V. Tassin, D. Pesme, M. C. Monteil, P. E. Masson-Laborde, C. Baccou, P. Fremerye, F. Philippe, P. Seytor, D. Teychenne, W. Seka, J. Katz, R. Bahr, and S. Depierreux, Phys. Rev. Lett. **116**, 235002 (2016).
[9] C. Z. Xiao, H. B. Zhuo, Y. Yin, Z. J. Liu, C. Y. Zheng, Y. Zhao, and X. T. He, Plasma Phys. Controlled Fusion **60**, 025020 (2018).
[10] C. Z. Xiao, H. B. Zhuo, Y. Yin, Z. J. Liu, C. Y. Zheng, and X. T. He, Phys. Plasmas **26**, 062109 (2019).
[11] S. J. Yang, H. B. Zhuo, Y. Yin, Z. J. Liu, C. Y. Zheng, X. T. He, and C. Z. Xiao, Phys. Rev. E **102**, 013205 (2020).
[12] C. Labaune, H. A. Baldis, E. Schifano, B. S. Bauer, A. Michard, N. Renard, W. Seka, J. D. Moody, and K. G. Estabrook, Phys. Rev. Lett. **76**, 3727 (1996).
[13] C. Labaune, H. A. Baldis, B. Cohen, W. Rozmus, S. Depierreux, E. Schifano, B. S. Bauer, and A. Michard, Phys. Plasmas **6**, 2048 (1999).
[14] W. Seka, H. A. Baldis, J. Fuchs, S. P. Regan, D. D. Meyerhofer, C. Stoeckl, B. Yaakobi, R. S. Craxton, and R. W. Short, Phys. Rev. Lett. **89**, 175002 (2002).
[15] C. S. Liu, M. N. Rosenbluth, and R. B. White, Phys. Rev. Lett. **31**, 697 (1973).
[16] C. S. Liu, M. N. Rosenbluth, and R. B. White, Phys. Fluids **17**, 1211 (1974).
[17] M. A. Mostrom and A. N. Kaufman, Phys. Rev. Lett. **42**, 644 (1979).
[18] R. White, P. Kaw, D. Pesme, M. N. Rosenbluth, G. Laval, R. Huff, and R. Varma, Nucl. Fusion **14**, 45 (1974).
[19] C. S. Liu and M. N. Rosenbluth, Phys. Fluids **19**, 967 (1976).
[20] A. Simon, R. W. Short, E. A. Williams, and T. Dewandre, Phys. Fluids **26**, 3107 (1983).
[21] B. B. Afeyan and E. A. Williams, Phys. Fluids **28**, 3397 (1985).
[22] R. W. Short, Phys. Plasmas **27**, 042703 (2020).
[23] M. N. Rosenbluth, Phys. Rev. Lett. **29**, 565 (1972).
[24] R. L. Berger, Phys. Fluids **27**, 1796 (1984).
[25] J. Heading, *An Introduction to Phase Integral Methods* (Methuen, London, 1962).
[26] C. Z. Xiao, Q. Wang, and J. F. Myatt (unpublished).
[27] R. K. Follett, J. A. Delettrez, D. H. Edgell, V. N. Goncharov, R. J. Henchen, J. Katz, D. T. Michel, J. F. Myatt, J. Shaw, A. A. Solodov, C. Stoeckl, B. Yaakobi, and D. H. Froula, Phys. Rev. Lett. **116**, 155002 (2016).
[28] R. L. Berger, L. J. Suter, L. Divol, R. A. London, T. Chapman, D. H. Froula, N. B. Meezan, P. Neumayer, and S. H. Glenzer, Phys. Rev. E **91**, 031103(R) (2015).
[29] Q. Wang, C. Y. Zheng, Z. J. Liu, C. Z. Xiao, Q. S. Feng, H. C. Zhang, and X. T. He, Plasma Phys. Controlled Fusion **60**, 025016 (2018).
[30] Q. S. Feng, C. Y. Zheng, Z. J. Liu, L. H. Cao, Q. Wang, C. Z. Xiao, and X. T. He, Phys. Plasmas **26**, 052101 (2019).
[31] Q. Wang, C. Y. Zheng, Z. J. Liu, L. H. Cao, C. Z. Xiao, Q. S. Feng, C. S. Liu, and X. T. He, Plasma Phys. Controlled Fusion **61**, 085017 (2019).
[32] J. Li, S. Zhang, C. M. Krauland, H. Wen, F. N. Beg, C. Ren, and M. S. Wei, Phys. Rev. E **101**, 033206 (2020).
[33] X. T. He, J. W. Li, Z. F. Fan, L. F. Wang, J. Liu, K. Lan, J. F. Wu, and W. H. Ye, Phys. Plasmas **23**, 082706 (2016).

[34] K. Lan, J. Liu, Z. Li, X. Xie, W. Huo, Y. Chen, G. Ren, C. Zheng, D. Yang, S. Li *et al.*, Matter Radiat. Extremes **1**, 8 (2016).

[35] J. Zhang, W. M. Wang, X. H. Yang, D. Wu, Y. Y. Ma, J. L. Jiao, Z. Zhang, F. Y. Wu, X. H. Yuan, Y. T. Li, and J. Q. Zhu, Philos. Trans. R. Soc. A **378**, 20200015 (2020).